Supporting Information

Hard carbon with opened pore structure for enhanced sodium storage performance

Shunzhang You, ‡[a] Qiaobao Zhang, ‡[b], Junxiang Liu, [c] Qiang Deng, [a] Zhefei Sun, [b] Dandan Cao, [a] Tongchao Liu, *[c] Khalil Amine *[c] and Chenghao Yang *[a]

[a] Guangzhou Key Laboratory for Surface Chemistry of Energy Materials, New Energy Research Institute, School of Environment and Energy, South China University of Technology, Guangzhou 510006, P. R. China

E-mail: esyangc@scut.edu.cn

[b] Department of Materials Science and Engineering, College of Materials, Xiamen University, Fujian 361005, P. R. China

[c] Chemical Sciences and Engineering Division, ArgonneNational Laboratory, Lemont, IL 60439, USA.

E-mail: liut@anl.gov (T.L.); amine@anl.gov (K.A.)

‡ These authors contributed equally to this work.

Experimental Procedures

Preparation of OP-HC

The wasted wood was first crushed, washed in deionized (DI) water and 0.5 mol L^{-1} HCl at 120 °C for 3 h to remove impurities, and dried in 80 °C for 12 h. Then, 5 wt% of polyvinyl pyrrolidone (PVP, $(C_6H_9NO)_n$) was added to the sample and mixed homogenously by ball milling. The sample was pre-treated at 300 °C for 5 h, and then carbonized at 1500 °C in N_2 for 3 h to obtain the opened pore structured hard carbon (OP-HC). For comparison, the pristine hard carbon (HC) was prepared by the similar method without adding PVP.

The activation and prolysis process by adding of PVP to waste wood precursors at elevated temperature are ascribed as follows: PVP is decomposed at high temperature and generates oxidizing agents NO_2, H_2O and CO_2 to react with the carbon carbonized from waste wood, while will facilitate the activation process. Moreover, plentiful gas (NO_2, CO_2, CO) diffused from inside to surface of OP-HC leads to expend of the interlayer.

$$(C_6H_9NO)_n == xNO_2 + yCO_2 + zH_2O + mCO + nC \quad (1)$$

$$2NO_2 + 2C == 2CO_2 + N_2 \quad (2)$$

$$H_2O + C == 2CO + H_2 \quad (4)$$

$$CO_2 + C == 2CO \quad (3)$$

Materials Characterizations

Microstructures of samples were investigated by using field-emission scanning electron microscopy (FESEM, Hitachi SU8010) and transmission electron microscopy (TEM, JEM-2100Plus). Crystal structures of samples were demonstrated by utilizing X-ray powder diffraction (XRD, Bruker D8, Cu Kα). Nitrogen adsorption experiments and micropore analysis were conducted at 77 K using Autosorb iQ apparatus. Small angle X-ray scattering (SAXS) from a SAXSess mc2 (Anton Paar) with a Cu Kα source. True density tests were performed on a JZ-1 Powder compaction density meter (Chengdu Jingxin Powder Testing Equipment Co., Ltd). Raman spectra of the samples were captured using a Horiba Raman spectrophotometer (LabRAM HR Evolution, Horiba) equipped with a Diode Pump Solid State Laser. Fourier transform infrared reflection (FTIR) spectra were collected by a FTIR spectrometer (Nicolet 6700, ThermoFisher Scientific). X-ray photoelectron spectroscopy (XPS, Escalab Xi+) was used to measure the chemical states of anode surface. The roughness and force curve of cycled anodes were observed by atomic force microscope (AFM, NTEGRA Spectra, Russia NT-MDT).

Electrochemical Measurements

Electrochemical properties of HC and OP-HC as SIB anodes were investigated by using 2032 coin-type half cells, with Na metal foils as counter and reference electrode. OP-HC, super P and carboxyl methyl cellulose (CMC) was mixed with a mass ratio of 96 : 2 : 2 in distilled water to obtain slurry. Coat the slurry on the copper foil and dry it in an oven at 80 °C overnight. The mass loading of OP-HC electrode is about 3-4 mg cm^{-2}. A Na foil was used as the counter electrode, 1 M $NaCF_3SO_3$ (NaOTF) in Diethylene glycol dimethyl ether (DEGDME) as the electrolyte and glass fiber as the separator. Both half and full cells were assembled in an argon glove box. Charge and discharge tests were performed on a LAND CT2001 battery testing system at 27 °C and cycled at different current densities with a voltage range of 0.01-2.5 V. Electrochemical impedance spectroscopy and CV tests were performed at CHI660e electrochemical workstation. The parameters of GITT were set with current pulse duration of 20 min at 0.1 C and an interval time of 3 h.

The coefficient diffusion of Na^+ ions measured from CV is calculated as follow:

$$I_p = (2.69 \times 10^5) n^{3/2} A D^{1/2} C v^{1/2}$$

Where I_p is the peak current (A), n is the number of reaction electrons, A is the contact area between the electrolyte and electrode (cm^2), D is the diffusion coefficient Na^+ ions ($cm^2\ s^{-1}$), C is the concentration of Na^+ ions in the electrode (mol cm^{-3}), and v is the scan rate (V s^{-1}).

The coefficient diffusion of Na^+ ions measured from GITT is calculated by:

$$D = \frac{4}{\pi\tau}\left(\frac{m_B V_M}{M_B S}\right)^2 \left(\frac{\Delta E_s}{\Delta E_\tau}\right)$$

where τ (s) is the pulse time, S is the active surface area (cm^2), m_B (g), M_B (g mol^{-1}) and V_M ($cm^3\ mol^{-1}$) are the mass, molar mass, and molar volume of HC. ΔE_S (V) and ΔE_τ (V) are voltage change caused by current pulse and galvanostatic discharge, respectively.

To further evaluate the electrochemical performance of OP-HC, fabricated OP-HC was assembled into 18650 full cells with $NaNi_{1/3}Fe_{1/3}Mn_{1/3}O_2$ (NFM) as cathode, the cathode capacity : anode capacity is set to be 1.2 : 1.

***In-situ* Examinations**

In-situ XRD analysis was conducted on the Bruker D8 (Cu Kα) using Be foil as the X-ray penetrator and Cu mesh as current collector. The parameters of *in-situ* XRD setting for each scan of the 2θ range from 10° to 40° with a step size of 0.02° and a scanning rate of 0.2° min^{-1}. *In-situ* TEM was conducted on the Jeol 2100 TEM. The OP-HC was distributed on a Mo tip as the working electrode and Na metal was scratched on a Cu wire as the counter electrode. A thin layer of Na_2O was formed during the transfer

process. A potential bias of ±3 V was applied to drive the diffusion of Na^+, when a physical contact between the two electrodes. *In-situ* EIS tests were performed at room temperature over the frequency range of 1×10^5–0.01 Hz using an electrochemical workstation (ZAHNER e, Zahner, Germany). The charge and discharge processes were conducted in CC−CV mode with a current of 300 mA g^{-1} over a voltage range of 0.01 to 2.5 V.

Simulation Methods

All spin-calculations were conducted with DFT implemented in Vienna ab initio simulation package (VASP). The exchange-correlation interactions were described by the Perdew–Burke–Ernzerhof within the generalized gradient approximation functional (GGA), and the corresponding energy cutoff and force tolerance are 500 eV and 0.02 eV Å-1, respectively. In this work, the 6×6×1 supercells were adopted to study the binding energy of sodium atoms with the k-point grids of 2×2×1. In addition, the Grimme dispersion correction (D3) is taken into account so as to resolve the van der Waals interactions. And the binding energy can be calculated by the following formula:

$$\Delta E = E(Na - HC) - E(Na) - E(HC)$$

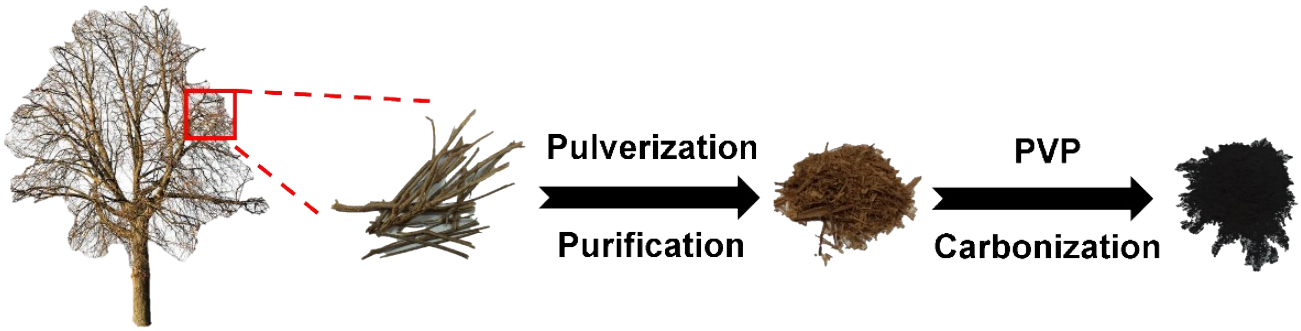

Figure S1. Schematic illustration of the synthesis process of OP-HC.

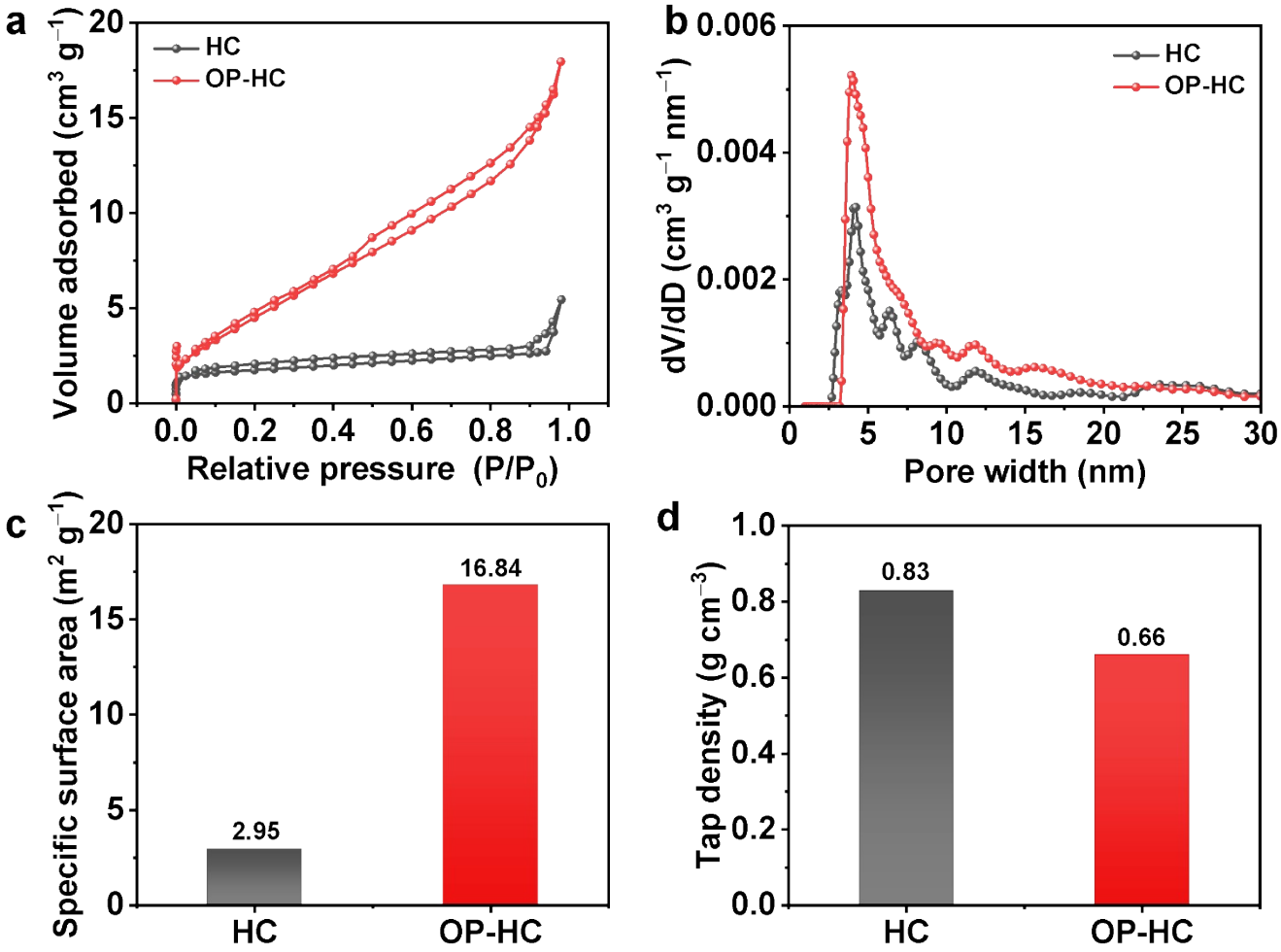

Figure S2. N_2 adsorption-desorption isotherms of HC and OP-HC (a). Pore size distribution of HC and OP-HC (b). Specific surface area (c) and tap density (d).

The specific surface area of OP-HC is 16.84 m^2 g^{-1}, and that of HC is 2.95 m^2 g^{-1}. While, HC and OP-HC exhibit a tap density of 0.83 and 0.66 g cm^{-3}, respectively.

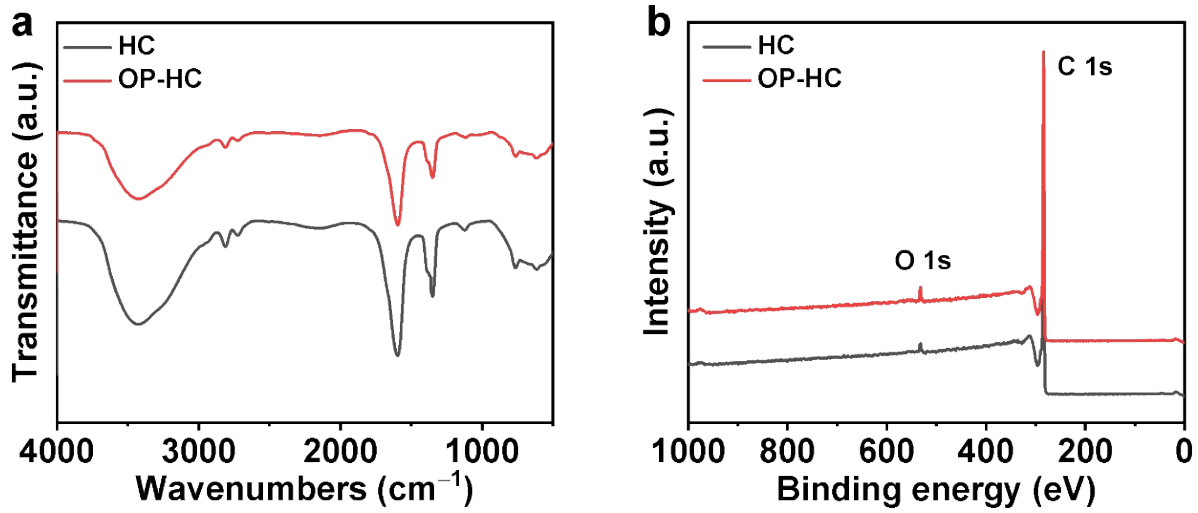

Figure S3. FTIR spectra (a), XPS spectra (b) of HC and OP-HC.

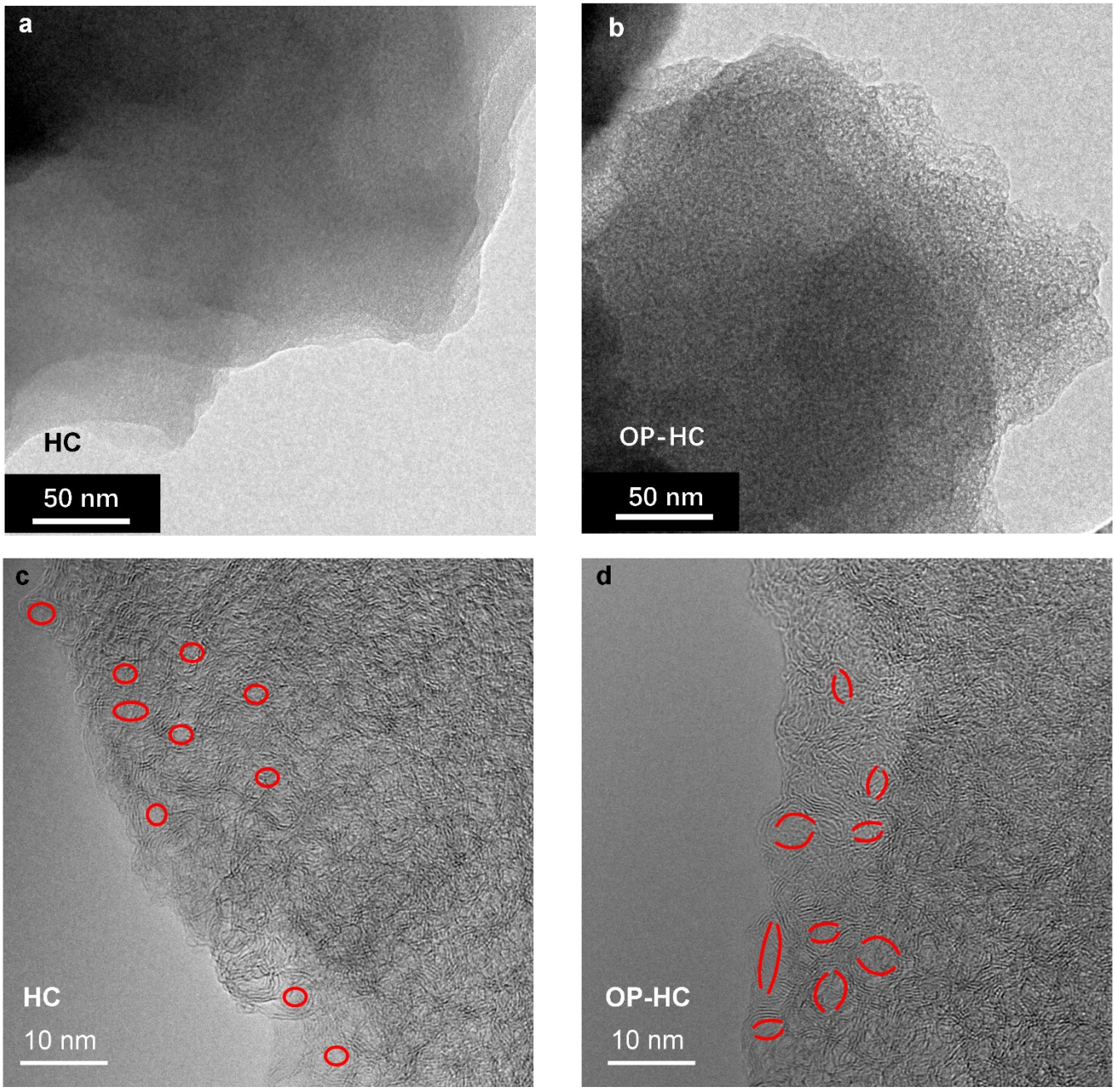

Figure S4. TEM images of HC (a) and OP-HC (b). HRTEM images of HC (a) and OP-HC (d).

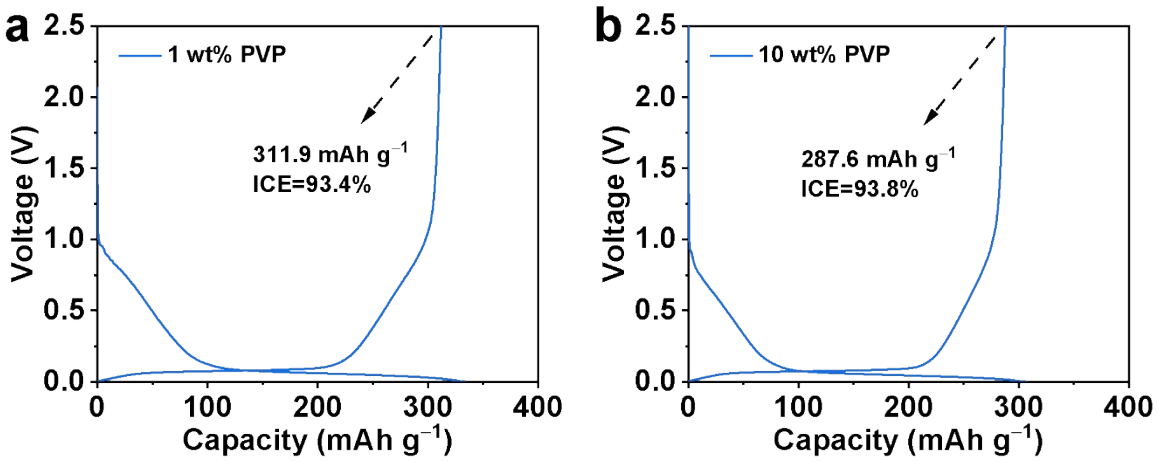

Figure S5. Charge/discharge profiles of the first cycle at 0.05 C of OP-HC prepared by adding with (a) 1 wt% and (b) 10 wt% PVP.

We tried to prepare hard carbon by adding three ratios of 1 wt%, 5 wt%, and 10 wt% to the precursor, but the performance of hard carbon prepared with only 5 wt% was improved. The reason for this is that 1 wt% PVP does not allow the pore structure to open, and 10 wt% PVP creates other types of hard carbon, resulting in an irreversible capacity increase.

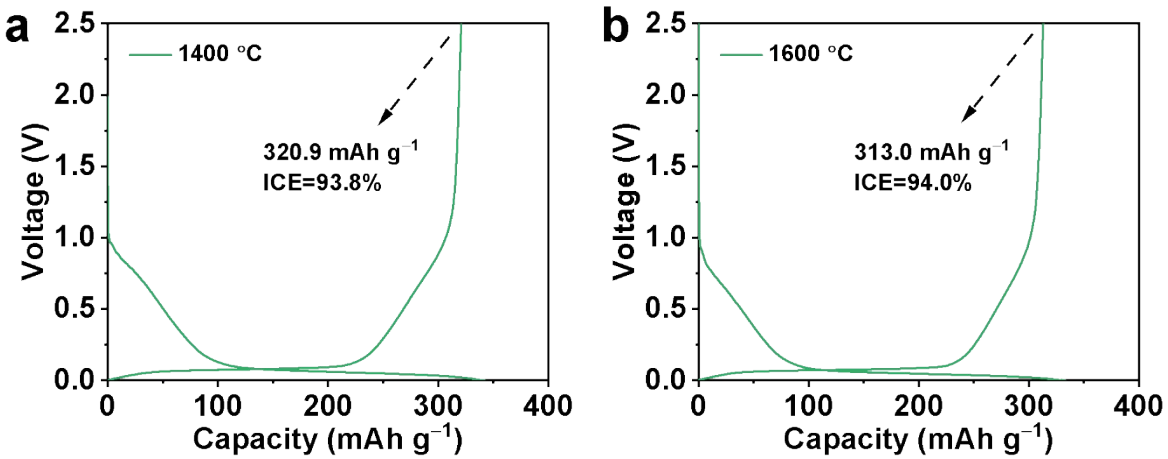

Figure S6. Charge/discharge profiles of the first cycle at 0.05 C of OP-HC carbonized at (a) 1400 °C and (b) 1600 °C.

We synthesized OP-HC at other high temperatures and assembled it into a battery for testing. As shown in **Figure S6**, the reversible capacity of OP-HC prepared at 1400 °C and 1600 °C decreased in the initial cycle, indicating that other high temperatures can affect the formation of opened pores and reduce sodium storage capacity.

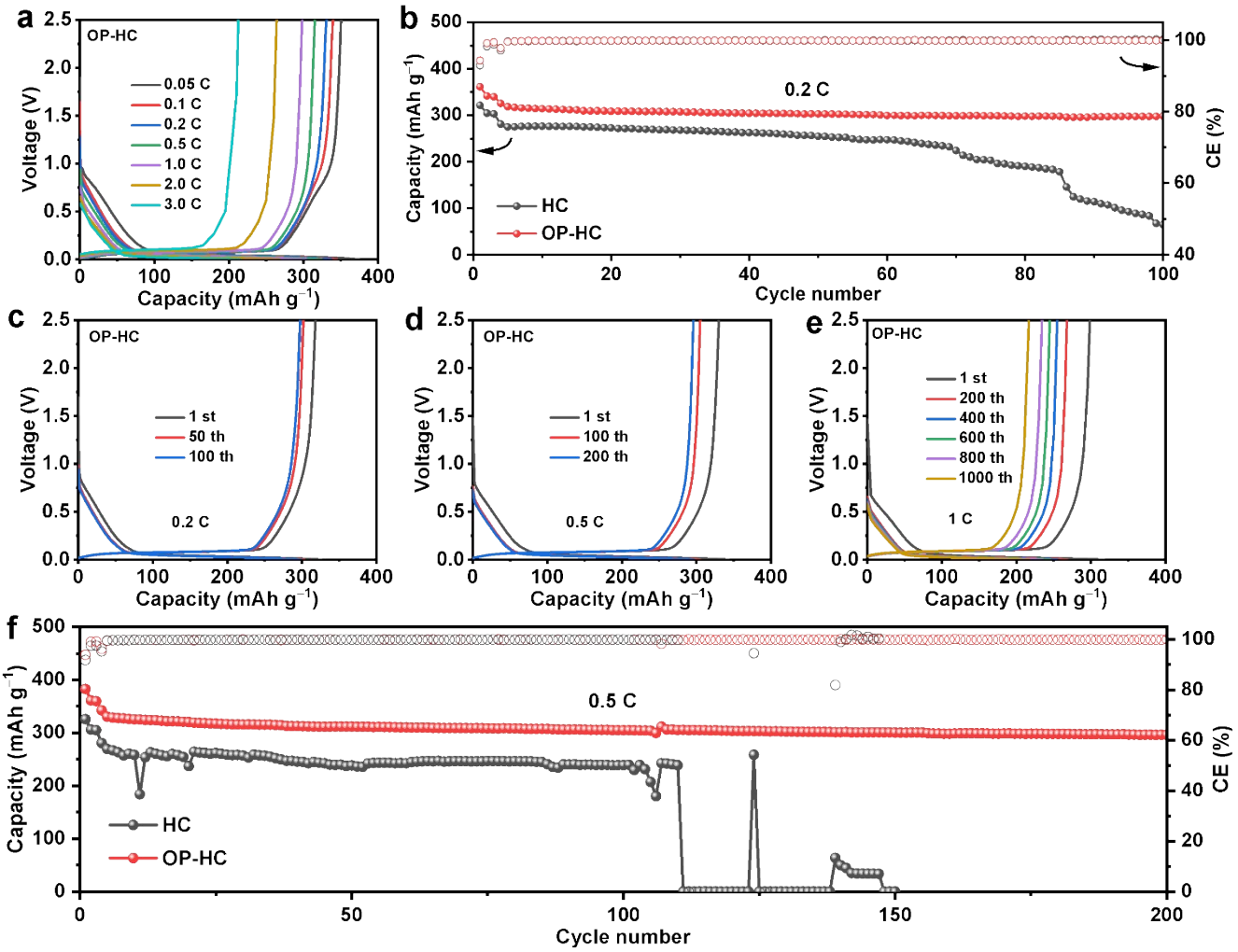

Figure S7. Discharge/charge curves (a) of OP-HC from 0.05 to 3.0 C. Cycling performance of HC and OP-HC anode at 0.2 C (b) and 0.5 C (f). Charge/discharge curves at different cycles of OP-HC anode at 0.2 C (c), 0.5 C (d) and 1.0 C (e).

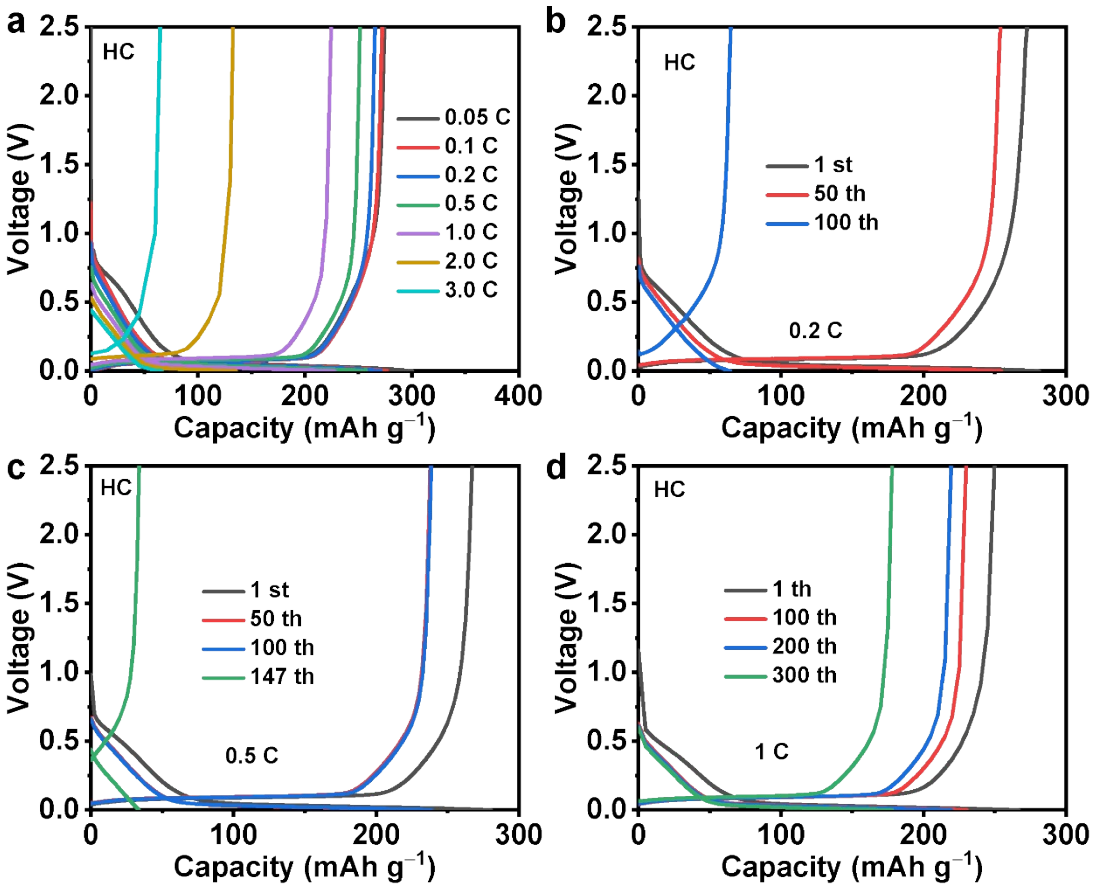

Figure S8. Charge/discharge curves at different current densities of HC (a). Charge/discharge curves at different cycles of HC anode at 0.2 C (b), 0.5 C (c) and 1.0 C (d).

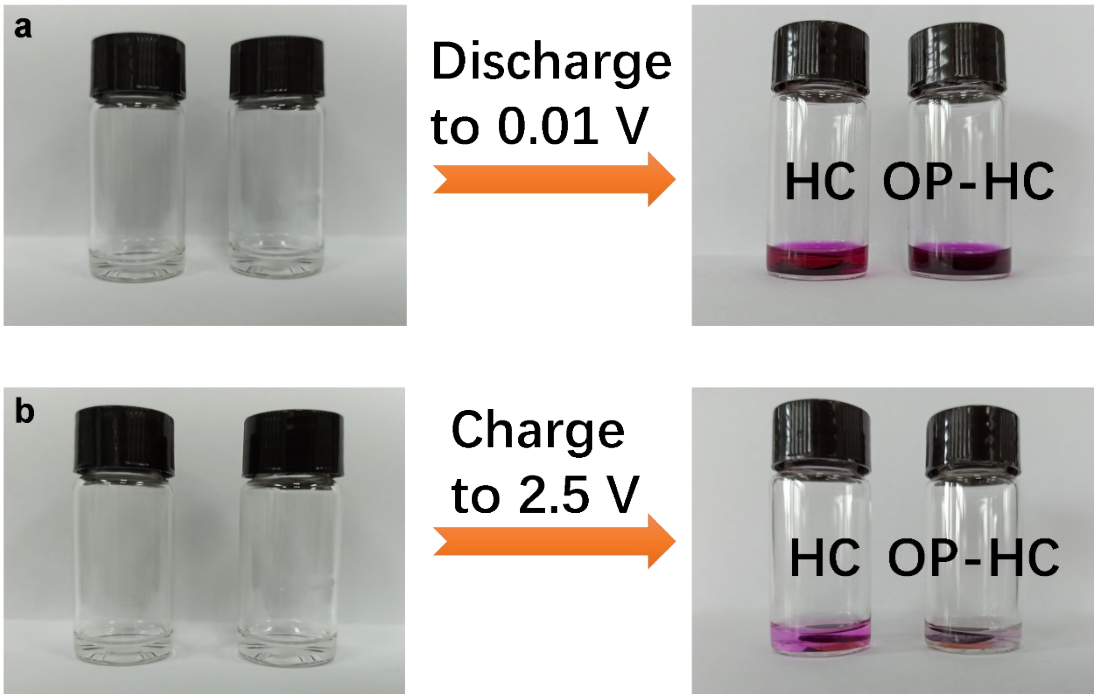

Figure S9. The optical photograph of HC and OP-HC electrodes when it is discharged to 0.01 V (a) and charged to 2.5 V (vs. Na^+/Na) (b) soaked in the ethanol solution containing 1 wt% phenolphthalein for 5 min.

Phenolphthalein reagent was used to directly study the present of metallic Na in HC and OP-HC during the charging/discharging process. Comparing with HC, color for the phenolphthalein solution of OP-HC anode discharged to 0.01 V is deeper, indicating that OP-HC can accommodation more metallic Na. When charged to 2.5 V, the phenolphthalein solution of OP-HC electrode is almost transparent, indicating that metallic Na in OP-HC are almost completely released. While, the deep purple color of the phenolphthalein solution for HC anode after charged to 2.5 V shows the existence of dead Na in it.

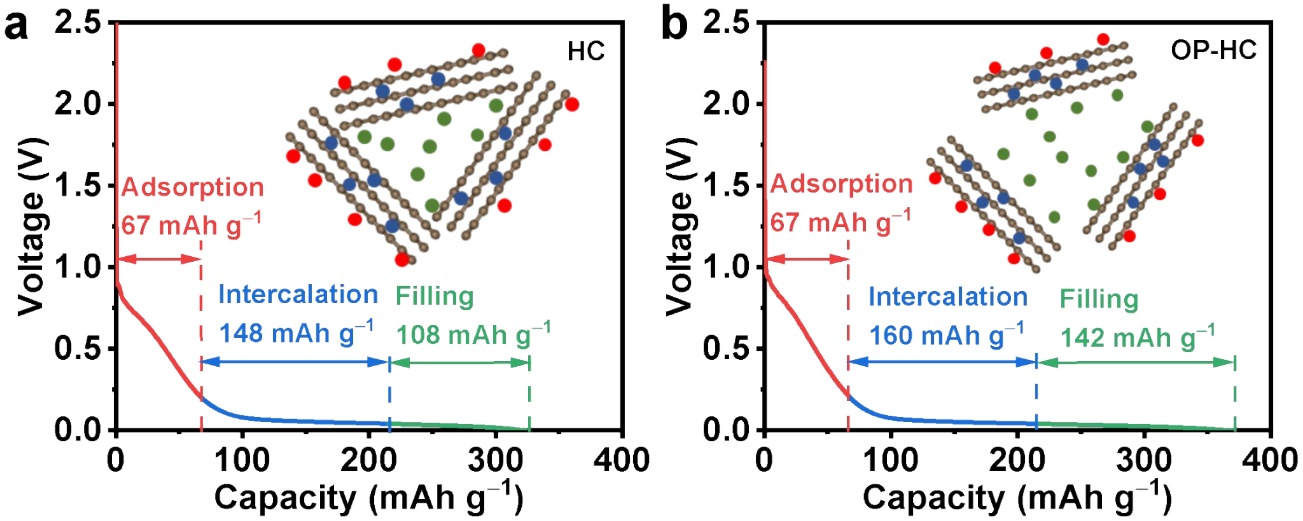

Figure S10. Schematic models of the adsorption-intercalation-filling mechanism for Na^+ ions storage in HC (a) and OP-HC (b).

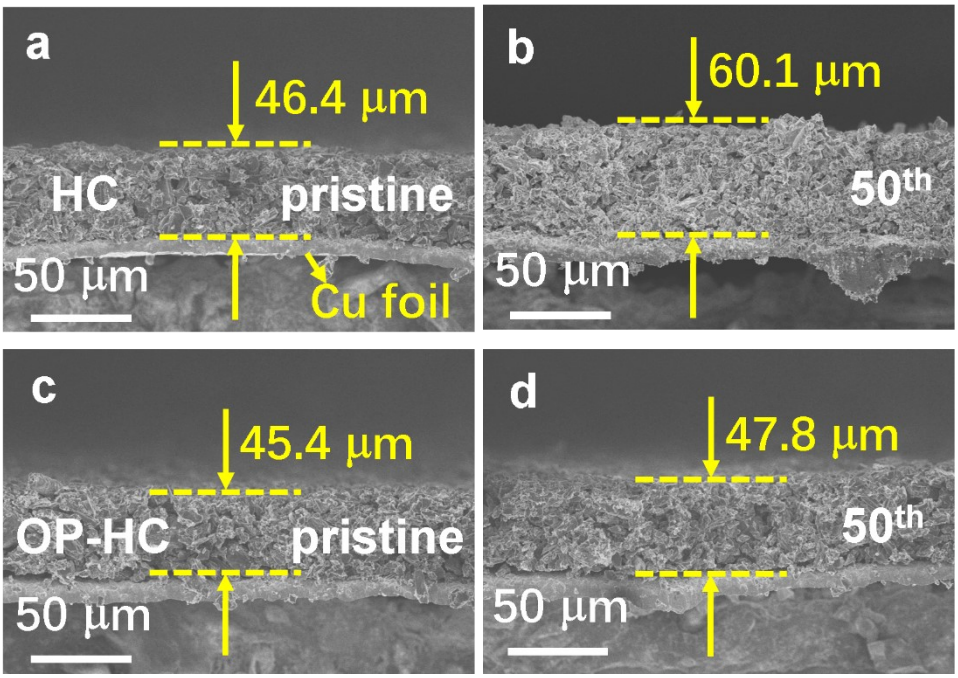

Figure S11. Sideview SEM images of HC (a, b) and OP-HC (c, d) anodes before and after 50 cycles at 0.2 C.

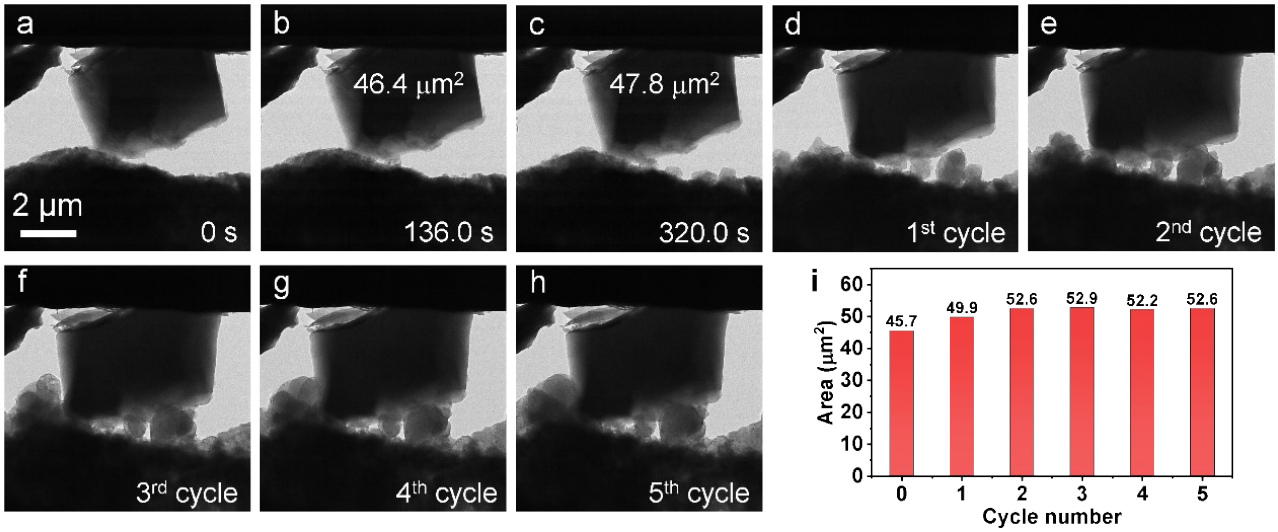

Figure S12. *In-situ* TEM images of sodiation/desodiation to the HC (a-h) and corresponding areal change of HC particles in the first five cycles (i).

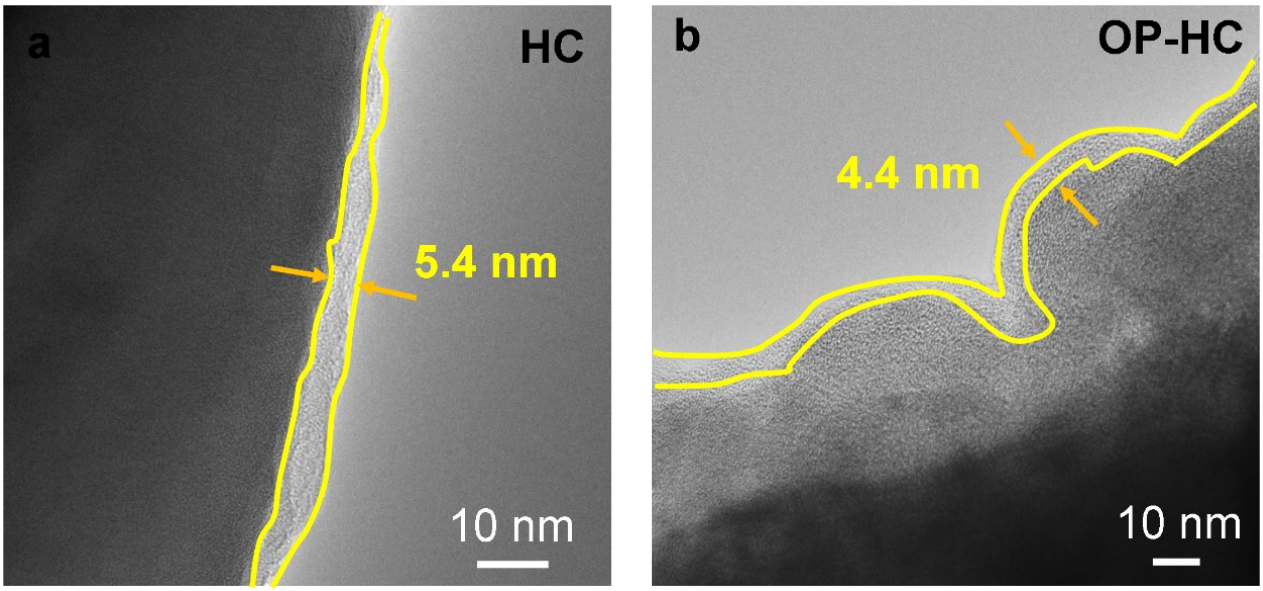

Figure S13. TEM images of HC (a) and OP-HC (b) anode after 50 cycles at 0.2 C.

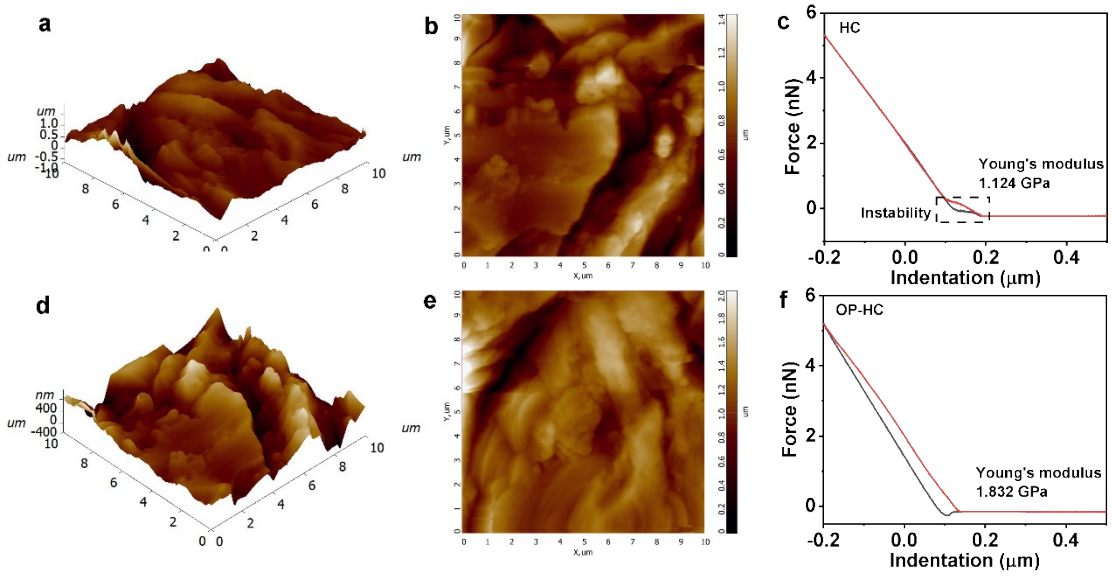

Figure S14. AFM images and force-displacement curves of HC(a-c) and OP-HC (d-f) anode cycled after 50th cycle at 0.2 C.

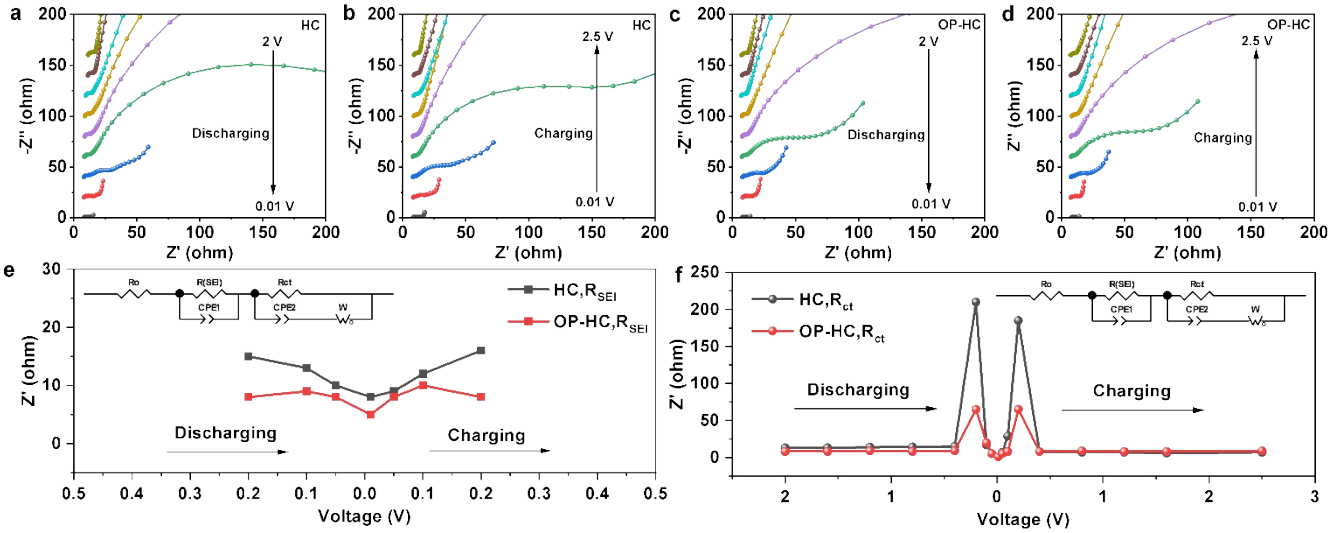

Figure S15. *In-situ* EIS profiles of the initial cycle during the charge and discharge process of HC (a, b) and OP-HC (c, d). The variation of R_{SEI} (e) and Rct (f) under different voltages. Inset in Figure (e, f) are the equivalent circuit diagrams.

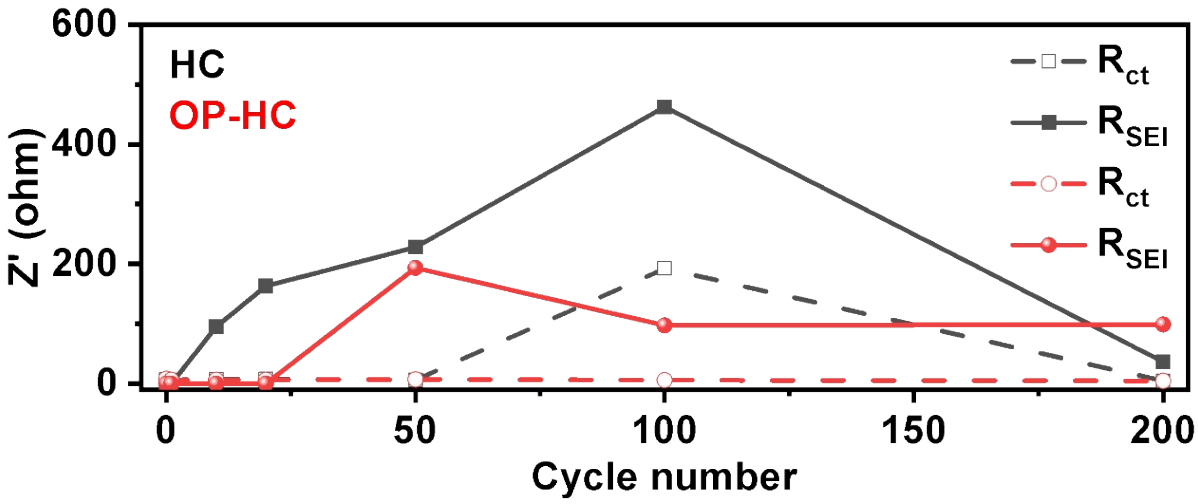

Figure S16. Evolution of R_{ct} and R_{SEI} after different cycles of HC and OP-HC anode. (R_{ct}, charge transfer resistance; R_{SEI}, interfacial resistance)

Table S1. Evolution of R_{ct} and R_{SEI} after different cycles of HC and OP-HC anode.

		Pristine	1st	10th	20th	50th	100th	200th
HC	R_{ct}	7.103	6.037	7.234	7.616	6.055	192.6	4.464
	R_{SEI}	0	0	94.85	163	228	462.6	36.55
OP-HC	R_{ct}	7.783	6.003	6.055	6.152	7.116	5.748	4.537
	R_{SEI}	0	0	0	0	193.6	97.25	98.83

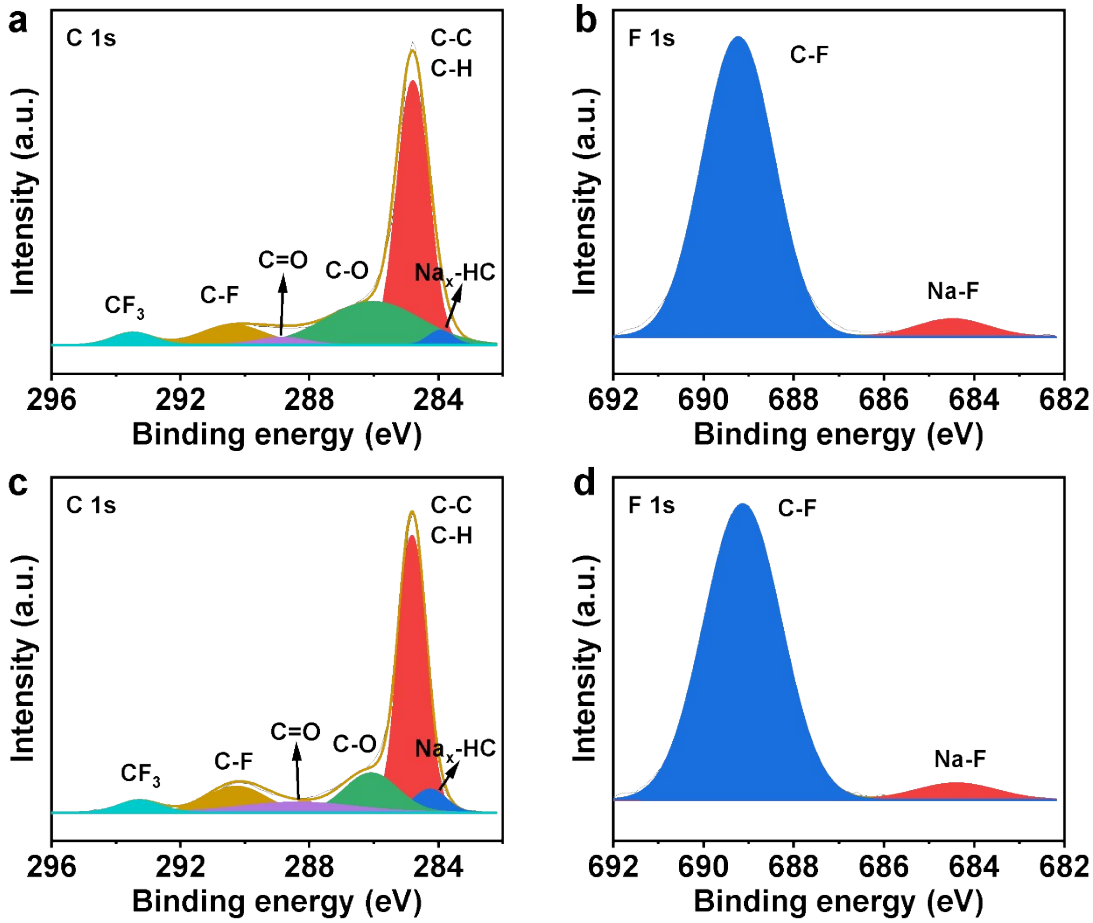

Figure S17. High-resolution XPS profiles of the HC (a, b) and OP-HC (c, d) anode cycled after 50 cycles at 0.2 C.

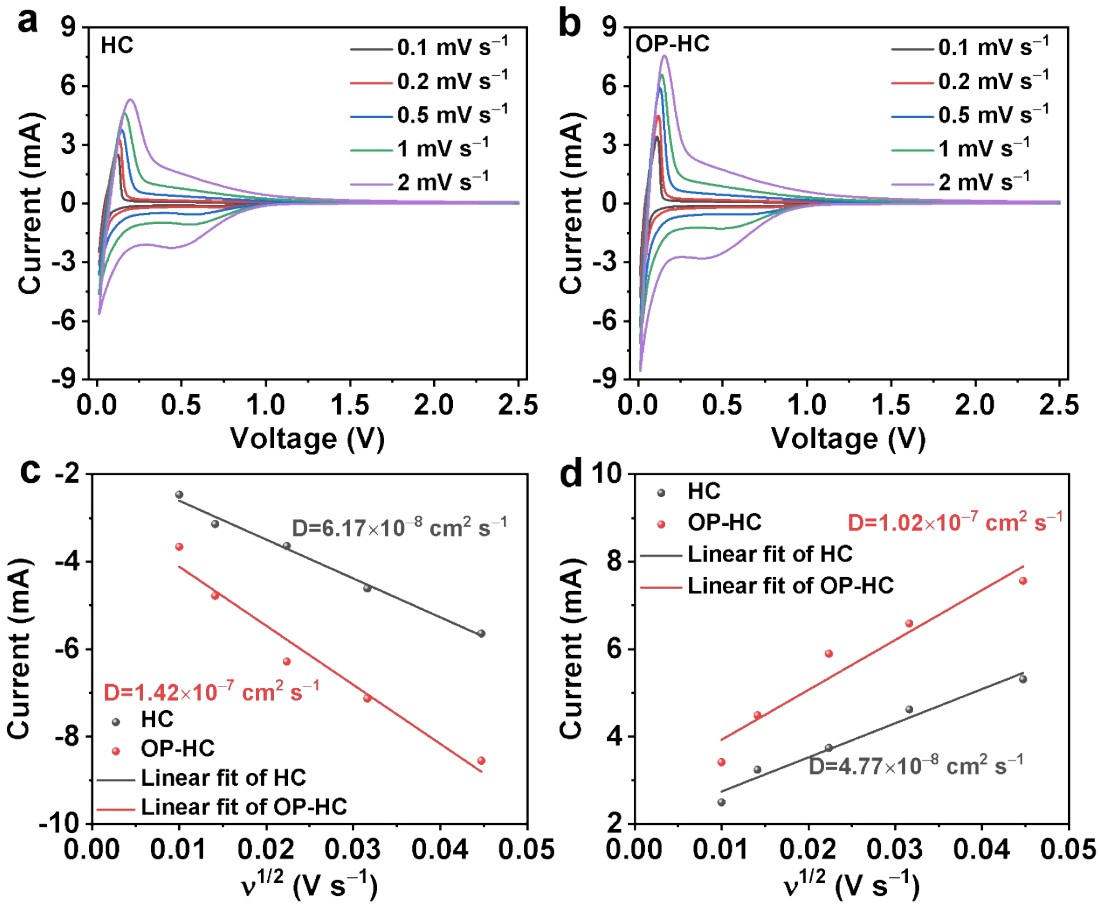

Figure S18. CV curves of HC (a) and OP-HC (b) under various sweep rates. The relationship between the peak current (I_p) and the square root over scan rate ($\nu^{1/2}$) of HC (c) and OP-HC (d).

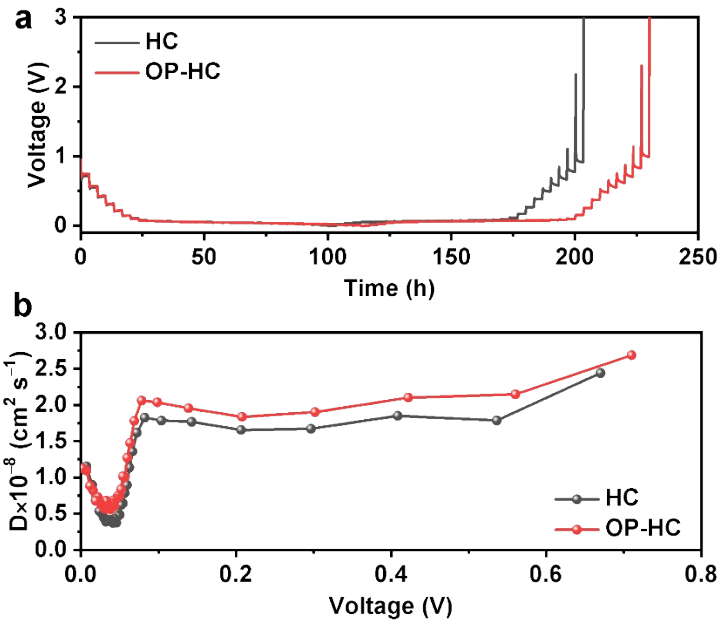

Figure S19. (a) GITT curves and (b) apparent diffusion coefficients D_{Na+} calculated from GITT results of HC and OP-HC.

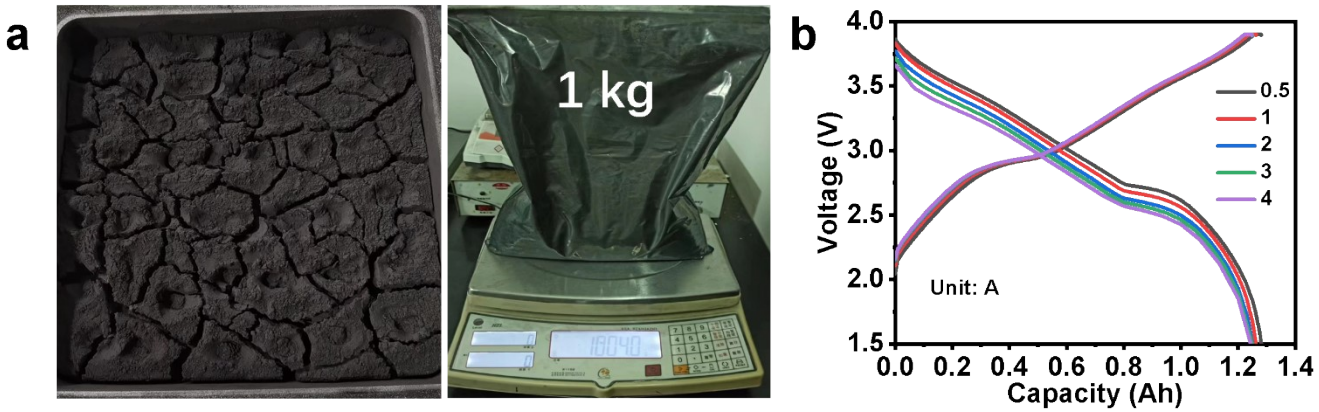

Figure S20. Optical photos for production capability of OP-HC in kg-level (a). Charge/discharge profiles (b) for the full cell at 0.5, 1.0, 2.0, 3.0 and 4.0 A.

Table S2. Comparisons of initial electrochemical performance for HC anodes.

Anode	Electrolyte	Average loading (mg cm^{-2})	Current density (mA g^{-1})	Charge/ Discharge capacity (mAh g^{-1})	ICE	Ref.
HAHC-1500	1 M $NaPF_6$ in DME	0.8-1.2	50	293/490	55%	S1
HC-1600	1 M $NaPF_6$ in EC:DMC (1:1 v:v)	3	18.6	306/351	87%	S2
HCF	1 M $NaPF_6$ in DME	-	50	342.6/390.2	87.8%	S3
HC-M	1 M $NaPF_6$ in EC:DMC (1:1 v:v) with 2vol% FEC	2-3	37.2	304.3/358.8	84.8%	S4
G1500	1 M $NaPF_6$ in EC:DMC (1:1 v:v)	-	30	287/338	85%	S5
FC1300	1 M $NaPF_6$ in DEGDME	-	10	291.0/329.8	88.2%	S6
HC-GLC	1 M $NaClO_4$ in EC:DEC (1:1 v:v)	5-6	20	343/361	95%	S7
Mg-Glu	1 M $NaClO_4$ in EC:DEC:PC (1:1:1 v:v:v)	1.5	20	367.1/460.6	79.7%	S8
HC/VC-1300	1 M $NaClO_4$ in PC with 5vol% FEC	0.8-1.2	100	278/379	68.7%	S9
MnHC	1 M $NaPF_6$ in EC:DEC (1:1 v:v)	1.1-1.6	20	336.8/366.1	92%	S10
HC-CS-A/PEO	1 M $NaPF_6$ in EC:DMC (1:1 v:v)	1.22	50	343.9/409.4	84%	S11
H300-1100	1 M $NaClO_4$ in EC:DEC (1:1 v:v)	-	20	369.8/448.2	82.5	S12
HCNS	1 M NaSO3CF3 in DEGDME	1	100	363.8/442.0	82.3%	S13
HC-1200M	1 M NaClO4 in PC with 5vol% FEC	-	50	323.6/513.6	63%	S14
OP-HC	**1 M $NaSO_3CF_3$ in DEGDME**	**3~4**	**15**	**350.7/369.1**	**95%**	**This work**

Note: HAHC stands for hard carbon (HC) fabricated by using sulfamethazine, HCF is hard carbon fiber, HC-M is HC synthesized from myrobalan extract, G stands for HC prepared by hydrothermal carbonization of glucose, FC is HC fabricated by using Fungus-pretreated basswood, HC-GLC is HC with large area graphite-like crystals, Mg-Glu is HC fabricated by using Mg glucose, HC/VC is HC spheres modified by vanadium carbide, CS-A/PEO is HC fabricated by using chondroitin sulfate A and ionic-conductor polyethylene oxide, HCNS is monodispersed HC nanospheres.

Table S3. Comparisons of cycled electrochemical performance for HC anodes.

Anode	Electrolyte	Cycle number	Current density (mA g^{-1})	Charge capacity (mAh g^{-1})	Capacity retention	Ref.
HAHC-1500	1 M $NaPF_6$ in DME	200	100	230	83%	S1
HCF	1 M $NaPF_6$ in DME	100	100	293.2	95.2%	S3
HC-M	1 M $NaPF_6$ in EC:DMC (1:1 v:v) with 2vol% FEC	44	372	286	82%	S4
FC1300	1 M $NaPF_6$ in DEGDME	500	200	221.6	86.4%	S6
HC-GLC	1 M $NaClO_4$ in EC:DEC (1:1 v:v)	100	150	234.6	93.5%	S7
HC/VC-1300	1 M $NaClO_4$ in PC with 5vol% FEC	100	100	261	93.8%	S9
HC-CS-A/PEO	1 M $NaPF_6$ in EC:DMC (1:1 v:v)	150	50	312	94%	S11
H300-1100	1 M $NaClO_4$ in EC:DEC (1:1 v:v)	100	100	250	87.6	S12
HCNS	1 M NaSO3CF3 in DEGDME	400	100	337	92.6%	S13
HC-1200M	1 M NaClO4 in PC with 5vol% FEC	500	50	310.4	60.5%	S14
OP-HC	**1 M $NaSO_3CF_3$ in DEGDME**	**200** **600**	**150** **300**	**296.1** **252.8**	**86.4%** **80%**	**This work**

Table S4. Comparisons of electrochemical performance for full cells.

Cathode	Anode	Electrolyte	Cycle number	Capacity retention	Ref.
$Na_3V_2(PO_4)_3$	HC-1600	1 M $NaPF_6$ in EC:DMC (1:1 v:v)	50	82%	S2
$Na_3V_2(PO_4)_3$	HCF	1 M $NaPF_6$ in DME	300	75%	S3
NaNMT	FC1300	1 M $NaPF_6$ in DEGDME	100	70.6%	S6
$Na_3V_2(PO_4)_3$	MnHC	1 M $NaPF_6$ in EC:DEC (1:1 v:v)	100	64.7%	S10
$Na_3V_2(PO_4)_3$	HC-CS-A/PEO	1 M $NaPF_6$ in EC:DMC (1:1 v:v)	150	76%	S11
$Na_3V_2(PO_4)_3$	H300-1100	1 M $NaClO_4$ in EC:DEC (1:1 v:v)	55	85.2%	S12
P2-$Na_{2/3}Ni_{1/3}Mn_{2/3}$ O_2	HCNS	1 M NaSO3CF3 in DEGDME	400	68%	S13
$Na_{1.6}VPO_{4.8}F_{0.7}$	WB-HC	1 M $NaPF_6$ in EC:PC (1:1 v:v)	100	89%	S15
NFPP	H-1500	1 M $NaPF_6$ in DME	100	83.6%	S16
NFM	**OP-HC**	**1 M $NaSO_3CF_3$ in DEGDME**	**400**	**94.5%**	**This work**

References

S1 Z. Huang, X. Qiu, C. Wang, W. Jian, L. Zhong, J. Zhu, X. Zu and W. Zhang, *J. Energy Storage*, 2023, **72**, 108406.

S2 H. Tonnoir, D. Huo, R. L. S. Canevesi, V. Fierro, A. Celzard and R. Janot, *Mater. Today Chem.*, 2022, **23**, 100614.

S3 N. Jiang, L. Chen, H. Jiang, Y. Hu and C. Li, *Small*, 2022, **18**, 2108092.

S4 A. Beda, A. M. Escamilla-Pérez, L. Simonin and C. Matei Ghimbeu, *ACS Appl. Energy Mater.*, 2022, **5**, 4774-4787.

S5 H. Au, H. Alptekin, A. C. S. Jensen, E. Olsson, C. A. O'Keefe, T. Smith, M. Crespo-Ribadeneyra, T. F. Headen, C. P. Grey, Q. Cai, A. J. Drew and M.-M. Titirici, *Energy Environ. Sci.*, 2020, **13**, 3469-3479.

S6 P. Wang, Y.-J. Guo, W.-P. Chen, H. Duan, H. Ye, H.-R. Yao, Y.-X. Yin and F.-F. Cao, *Nano Res.*, 2023, **16**, 3832-3838.

S7 X. Li, J. Sun, W. Zhao, Y. Lai, X. Yu and Y. Liu, *Adv. Funct. Mater.*, 2022, **32**, 2106980.

S8 X. Chen, J. Tian, P. Li, Y. Fang, Y. Fang, X. Liang, J. Feng, J. Dong, X. Ai, H. Yang and Y. Cao, *Adv. Energy Mater.*, 2022, **12**, 2200886.

S9 P. Xiong, Y. Kang, N. Yao, X. Chen, H. Mao, W.-S. Jang, D. M. Halat, Z.-H. Fu, M.-H. Jung, H. Y. Jeong, Y.-M. Kim, J. A. Reimer, Q. Zhang and H. S. Park, *ACS Energy Lett.*, 2023, **8**, 1613-1625.

S10 J. Zhao, X.-X. He, W.-H. Lai, Z. Yang, X.-H. Liu, L. Li, Y. Qiao, Y. Xiao, L. Li, X. Wu and S.-L. Chou, *Adv. Energy Mater.*, 2023, **13**, 2300444.

S11 W. Li, X. Guo, K. Song, J. Chen, J. Zhang, G. Tang, C. Liu, W. Chen and C. Shen, *Adv. Energy Mater.*, 2023, **13**, 2300648.

S12 M. Yang, J. Zhu, S. Bi, R. Wang and Z. Niu, *Adv. Mater.*, 2022, **34**, 2201744.

S13 Z. Chen, X. Li, D. Wang, Q. Yang, L. Ma, Z. Huang, G. Liang, A. Chen, Y. Guo, B. Dong, X. Huang, C. Yang and C. Zhi, *Energy Environ. Sci.*, 2021, **14**, 3492-3501.

S14 Z. Cao, X. Zhu, D. Xu, P. Dong, M. O. L. Chee, X. Li, K. Zhu, M. Ye and J. Shen, *Energy Storage Mater.*, 2021, **36**, 132-138.

S15 M. E. Lee, S. M. Lee, J. Choi, D. Jang, S. Lee, H.-J. Jin and Y. S. Yun, *Small*, 2020, **16**, 2001053.

S16 Z. Tang, R. Zhang, H. Wang, S. Zhou, Z. Pan, Y. Huang, D. Sun, Y. Tang, X. Ji, K. Amine and M. Shao, *Nat. Commun.*, 2023, **14**, 6024.